Presented at the IBM Seminar on Regional Groundwater Hydrology and Modeling, Venice, Italy, May 25-26, 1976

LBL-5209

Energy and Environment Division

Recent Developments In Modeling Groundwater Systems

T.N. Narasimhan and P.A. Witherspoon

May 20, 1977

Lawrence Berkeley Laboratory University of California/Berkeley

Prepared for the U.S. Energy Research and Development Administration under Contract No. W-7405-ENG-48

LBL-5209

For saturated flow problems it is convenient to use h as the dependent variable, whereas for problems including unsaturated flow or problems including system deformation, it is necessary to decouple the gravitational and pressure components of h and use ψ as the dependent variable. Before introducing the dependent variable, we shall adopt Darcy's law in the form (Philip, 1969)

$$\vec{q}_r = -\underline{\underline{K}}\nabla h \quad . \tag{4}$$

Inserting (4) into (1) and assuming, on empirical grounds, that M_w is a function only of h, we obtain

$$\rho_w GV + \int_\Gamma \rho_w \underline{\underline{K}}\nabla h \cdot n d\Gamma = \frac{dM_w}{dh} \frac{\partial h}{\partial t} \quad . \tag{5}$$

The amount of water contained in a finite subregion of volume V is given by

$$M_w = \rho_w V_v S \quad . \tag{6}$$

We therefore define a term called the "fluid mass capacity" of the subregion [Narasimhan and Witherspoon, 1976b]

$$M_c = \frac{d}{dh}[\rho_w V_v S] = V_v S \frac{d\rho_w}{dh} + \rho_w S \frac{dV_v}{dh} + \rho_w V_v \frac{dS}{dh} \tag{7}$$

Physically, M_c represents the amount of fluid mass that the finite subregion can absorb when the average head within the system changes by unity. The general equation of transient groundwater motion therefore takes the form

$$\rho_w GV + \int_\Gamma \rho_w \underline{\underline{K}}\nabla h \cdot \vec{n} d\Gamma = M_c \frac{\partial h}{\partial t} \quad . \tag{8}$$

Equation 8 is in an integral form. It is more customary in the literature to express (8) in a volume-normalized differential form. Thus, we shall first define a quantity "specific fluid mass capacity" as $m_c = M_c/V$, and then divide (8) by V and let the finite subregion become arbitrarily small to obtain

$$\rho_w G + \text{div}\,(\rho_w \underline{\underline{K}}\nabla h) = m_c \frac{\partial h}{\partial t} \quad , \tag{9}$$

where divergence is defined by (Sokolnikoff and Redheffer, 1966)

$$\text{div}\,\vec{q}_r = \lim_{V \to 0} \frac{1}{V} \int_\Gamma \vec{q}_r \cdot \vec{n} \cdot d\Gamma \quad . \tag{9a}$$

Under conditions when $\underline{\underline{K}}$ and m_c are strongly dependent on h, as in the case of unsaturated flow, it is mathematically more convenient to use moisture content θ as the dependent variable instead of h. Thus, soil physicists often use the governing differential equation

$$\rho_w G + \text{div}\,(\rho_w \underline{\underline{D}}\nabla\theta) = \frac{\partial \theta}{\partial t} \quad , \tag{10}$$

where

$$\underline{\underline{D}} = \underline{\underline{K}} \frac{dh}{d\theta} \quad \text{and} \quad \theta = nS \quad .$$

Equation 13 is generally of limited use since it is applicable only to systems composed of a single material (Klute, 1972).

For steady-state flow we let $\partial h/\partial t = 0$ and (9) reduces to Poisson's equation

$$\text{div}\,(\rho K \nabla h) = -\rho_w G \tag{11}$$

and in the absence of sources or sinks (11) further reduces to the Laplace equation

$$\text{div}\,(\rho_w K \nabla h) = 0 \quad . \tag{12}$$

In applying (8) to actual systems, the equation is appropriately modified to accommodate the special dependences of $\underline{\underline{K}}$ and M_c on h or to handle special conditions on the boundary. We will now proceed to examine the application of (8) to realistic systems, starting with the simplest case.

Confined Systems

The simplest system to consider is one in which the flow region is fully saturated and the material coefficients $\underline{\underline{K}}$ and M_c are independent of time. In such a system, M_c is governed only by the compressibility of water and that of the porous medium. As shown by Domenico (1972, p. 220), for fully saturated confined systems,

$$\rho_w GV + \int_\Gamma \rho_w \underline{\underline{K}}\nabla h \cdot n d\Gamma = V\gamma_w(\alpha + n\beta) \frac{\partial h}{\partial t} \quad . \tag{13}$$

The quantity $S_s = \gamma_w(\alpha + n\beta)$ is often referred to as specific storage in groundwater hydrology. Many workers have used (13) for modeling confined groundwater systems with fixed geometry (e.g. Fayers and Sheldon, 1962; Pinder and Bredehoeft, 1966; Javandel and Witherspoon, 1968; and Prickett and Lonnquist, 1971). Equation 13 has also been extended by some to include unconfined systems with the assumption that the position of the water table is known and fixed (e.g., Tysen and Weber, 1964; Freeze and Witherspoon, 1966). The source term in (13) has been used by different workers to simulate the effects of production wells, leakage from aquitards and streams, transfer of water to the atmosphere through evaporation, and infiltration due to rainfall (e.g., Prickett and Lonnquist, 1971).

The chief limitations of (13) are twofold. The first is that it ignores flow in the unsaturated zone. Secondly, it assumes a constant value of S_s, an assumption which may not be appropriate for systems experiencing large head changes over prolonged periods of time or for systems undergoing land subsidence. Since soil deformation is related to stress changes induced by variations in pore fluid pressure, Equation 13 cannot effectively handle time-dependent changes in S_s unless gravity is decoupled from fluid pressure and due consideration is given to the skeletal stress field.

The Free-Surface Approximation

Hydrogeologists and civil engineers often choose to neglect modeling the unsaturated zone so as to avoid the computational difficulties inherent in taking into account the complex dependence of $\underline{\underline{K}}$ and M_c on the pressure head ψ. Instead, using suitable approximating assumptions, the effect of the unsaturated zone is replaced by an equivalent boundary condition.

In the case of steady seepage in an unconfined system, it is often convenient to assume that the flow region is saturated, but that the exact location of the free surface is unknown. The mathematical problem then reduces to one of determining the position of a part of the boundary of the flow region (free surface) by trial and error, using the following boundary constraints

$$h = \xi$$
$$\text{and} \qquad \text{on the free surface.} \qquad (14)$$
$$\underline{\underline{K}}\nabla h \cdot \vec{n} = I n_3$$

This approach has been employed by Taylor and Brown (1967), Jeppson (1968), Neuman and Witherspoon (1970), Remson et al. (1971), Cheng and Li (1973), France (1974) and others.

In the case of nonsteady flow with a free surface, the free surface continuously changes position. To handle this feature, the simplifying assumption is made that the water is instantaneously released from the region through which the free surface is given by (Bear et al. 1968; Neuman and Witherspoon, 1971)

$$h = \xi$$
$$\text{and} \qquad \text{on the free surface.} \qquad (15)$$
$$\underline{\underline{K}}\nabla H \cdot \vec{n} = (I - S_y \frac{\partial \xi}{\partial t}) n_3$$

In most free-surface problems it is customary to assume that the saturated porous medium is rigid, that water is incompressible, and that the saturated flow region obeys the Laplace equation.

An added simplification used by civil engineers is the Dupuit (1863) assumption. That is, the hydraulic head is constant along any vertical line in the aquifer, and water moves only horizontally within the saturated zone.

For steady-state flow, the Dupuit assumption leads to the well-known Forchcheimer equation (Prickett, 1975)

$$\frac{\partial^2 (h^2)}{\partial x^2} + \frac{\partial^2 (h^2)}{\partial y^2} = 0 \quad . \qquad (16)$$

For nonsteady flow in a nonhomogeneous-isotropic aquifer, the Dupuit assumptions lead to (Prickett, 1975)

$$\frac{\partial}{\partial x}\left(Kh \frac{\partial h}{\partial x}\right) + \frac{\partial}{\partial y}\left(Kh \frac{\partial h}{\partial y}\right) = S_y \frac{\partial h}{\partial t} \quad . \qquad (17)$$

Equation 17 is also known as the Boussinesq equation and has been used by Pikul et al. (1974).

In writing (15) it was assumed that water is instantaneously released from storage in the region through which the water table is falling. To be more realistic, Boulton (1954) introduced the concept of delayed yield from storage to take into account the slow drainage of water from the unsaturated zone. The delayed-drainage concept has since been examined in detail by Neuman (1972), Streltsova (1972) and others.

Saturated-Unsaturated Flow

More realistic than the free-surface approximation is a groundwater flow model, which simultaneously considers flow in the saturated as well as the unsaturated zones. In general, saturated-unsaturated flow involves the consideration of two phases: water and air. A rigorous modeling of saturated-unsaturated flow should therefore involve setting up two mass conservation equations, one for water and one for air (Morel Seytoux, 1973). However, the model is usually simplified with the assumption that the air phase is continuous in the porous medium, and is at atmospheric pressure, thereby neglecting the mass-conservation equation for air.

The saturated-unsaturated flow equation differs from (13) in two respects. First, $\underline{\underline{K}}$ is a strong function of ψ in the unsaturated zone, and second, it includes a desaturation coefficient, $dS/d\psi$ in the fluid mass capacity term. Thus the saturated-unsaturated flow equation becomes (Freeze, 1971)

$$\rho_w \, GV + \int_\Gamma \rho_w \underline{\underline{K}}\nabla h \cdot \vec{n} d\Gamma$$
$$= V[\rho_w \, S(\alpha + n\beta) + \rho_w n \frac{\partial S}{\partial \psi}] \frac{\partial \psi}{\partial t} \qquad (18)$$

in which $\underline{\underline{K}}$ as well as $\partial S/\partial\psi$ are strong functions of ψ, characterized by hysteresis. Equation 18 is inherently nonlinear due to the variability of the material coefficients with ψ. It is often customary to assume that n is constant in the unsaturated zone and that $S_s = (\alpha + n\beta)$ is constant in the saturated zone. Then, neglecting small changes in ρ_w, we obtain the simple relation (Neuman, 1973b)

$$GV + \int_\Gamma \underline{\underline{K}} \, (z + \psi) \cdot \vec{n} d\Gamma = V[S_s + C] \frac{\partial \psi}{\partial t} \quad , \qquad (19)$$

where $C = \dfrac{\partial \theta}{\partial \psi}$.

Equation 18 is sometimes further simplified (Vauclin et al., 1975) by assuming that the saturated zone is incompressible. Thus

$$GV + \int_\Gamma \underline{\underline{K}}\nabla(z + \psi) \cdot n d\Gamma = VC \frac{\partial \psi}{\partial t} \quad . \qquad (20)$$

Consideration of unsaturated flow leads to some special boundary conditions involving the seepage face and the atmospheric boundaries. The seepage face is a boundary on which (Cooley, 1971; Neuman, 1973b; Narasimhan, 1975; Vauclin et al., 1975) $\psi = 0$ and further, the flux along the outer normal to the seepage face, $K\nabla(z + \psi) \cdot \vec{n} > 0$, meaning that flux can only leave the system across a seepage face.

Water can be lost from an unsaturated soil to the atmosphere either by evaporation or by evapotranspiration (Neuman, et al., 1975). The maximum amount of water that the atmosphere can remove from the soil is equal to the sum of potential evaporation and potential evapotranspiration, which must be determined from micrometeorological data. In addition, there also exist lower limits for the pressure heads that can develop either at the dry soil surface or at plant roots. The soil atmosphere boundary is therefore neither a prescribed potential boundary not a prescribed flux boundary, but is one on which an upper bound for flux and a lower bound for potential are prescribed.

An infiltration boundary is another boundary of interest. If the rate of infiltration at the surface exceeds the ability of the soil to transmit water, as determined by its saturated permeability, then part of the surface addition must be lost as runoff. Thus, an infiltration boundary has an upper limit for boundary flux.

The saturated-unsaturated models described above are of considerable practical use in representing materials of moderate to high saturation. However, the deficiency of these models (Equations 18-20) lies in the fact that they do not give due consideration to the mechanics of soil deformation.

Deforming Porous Media

Accurate modeling of soil deformation is important from the viewpoint of land subsidence due to groundwater withdrawal, as well as for considerations of long-range groundwater management. Experience with the behavior of unconsolidated soils suggests that soil properties such as compressibility and permeability may undergo nonreversible changes with time due to the nonelastic response of the soil to changes in loading (Gambolati and Freeze, 1973; Helm, 1974). As a result, both K and α in (13) become nonlinear coefficients. These nonlinearities are governed by the distribution of skeletal stresses in the soil and hence, in order to duly account for these nonlinearities, one must incorporate the stress field into the governing equation. In considering soil deformation in regional groundwater systems, the changes in regional tectonic stresses are generally ignored and the total stress on the system is assumed invariant in time. However, due to changes in pore fluid pressure caused by water movement, the skeletal stresses change with time causing soil deformation. The primary conceptual necessity in modeling deformation is therefore a relation between pore fluid pressure and skeletal stress.

Soil deformation is generally a three-dimensional phenomenon and a rigorous solution of the problem should consider solution of two independent governing equations -- one for fluid flow and another for stress-strain behavior, which are coupled through a criterion that assures compatibility of volume change (see for example, Sandhu and Wilson, 1969). However, in regional groundwater modeling, the consideration of the general stress-strain equation is usually avoided on grounds of effort and economy. Instead, making use of the basic concept of one-dimensional consolidation theory of Terzaghi, soil deformation is handled in an approximate fashion with the help of a single fluid-flow equation. The one-dimensional consolidation theory has been used for modeling groundwater systems by Gambolati and Freeze (1973), Helm (1975) and Narasimhan (1975).

The one-dimensional theory of deformation is ideally suited for systems in which lateral strains are negligible and all the deformation occurs in the vertical direction. Fundamental to this theory are the concepts of effective stress, σ' and its relation to pore water pressure given by

$$\sigma' = \sigma - \gamma_w \psi \quad . \tag{21}$$

However, some petroleum engineers (Robinson and Holland, 1970) believe that only part of the pore water pressure (the concept of boundary porosity) may influence σ'. Similar ideas have also been expressed by Bishop (1959) and McMurdie and Day (1960) in attempting to relate negative pore pressure and effective stress in the unsaturated zone. Thus,

$$\sigma' = \sigma - \chi\gamma_w\psi \ , \quad 0 \leq \chi \leq 1 \quad . \tag{22}$$

The parameter χ can especially be a function of ψ in the unsaturated zone. Assuming σ = constant and $\chi = \chi(\psi)$, we obtain

$$\frac{d\sigma'}{d\psi} = - \gamma_w \chi' \quad , \tag{23}$$

where

$$\chi' = [\chi + \psi \frac{d\chi}{d\psi}] \quad . \tag{24}$$

The principal task in applying (8) to a deformable porous medium is to evaluate the quantity dV_v / dh occurring in the fluid mass capacity term on the right hand side of (7). Since $h = z + \psi$ and since both z and ψ may vary with time in a deformable porous medium, it is advantageous to make the reasonable assumption that z does not vary appreciably in any given interval of time and hence can be handled as a temporal step function. Then, in the light of (24) we can write

$$\frac{d(V_v)}{dh} = \frac{d(V_v)}{d\psi} = \frac{d(V_v)}{d\sigma'} \frac{d\sigma'}{d\psi} = - \chi' \gamma_w \frac{d(V_v)}{d\sigma'} \tag{25}$$

Another point to remember here is that Darcy's law describes the velocity of water relative to the velocity of grains (e.g. Philip, 1969). The dependence of Darcy's law on grain velocity as well as the fact that the elemental volume itself varies with time, requires a precise definition of the nature of the volume element for which the conservation equation is written and the reference coordinate system. These questions have been examined by Cooper (1966), Smiles and Rosenthal (1968), Philip (1969), Verruijt (1969), Gambolati (1973a,b), Cooley (1975) and others. Essentially, the problem can be approached in two different ways: (a) the Eulerian approach using a fixed coordinate system, in which the bulk volume of the elemental volume is constant in time; or (b) the Lagrangian approach using a material coordinate system, in which the elemental volume has constant volume of soil particles, and in which the soil particles remain at rest. Jacob's (1950) classical development of the equation of groundwater flow, as pointed out by De Wiest (1969), related to a hybrid elemental volume, which was treated in a Eulerian fashion in the space domain and in a Lagrangian fashion in the time domain.

According to Gambolati (1973b), the one-dimensional flow equation for a fixed element in fixed coordinates should read

$$\frac{k}{\gamma_w} \frac{\partial^2 p}{\partial z^2} = \{[(P \frac{d\alpha}{dp} + \alpha)/(1 + \alpha p)] + n\beta\} \cdot [\frac{\partial p}{\partial t} + v_g \frac{\partial p}{\partial z}] - \frac{k\beta}{\gamma_w} (\frac{\partial p}{\partial z})^2 - 2KS \frac{\partial p}{\partial z} \ . \tag{26}$$

During the mid-1960s, structural engineers devoted much of their time to the development of an integral method which, unlike the IFDM, would be capable of handling general tensorial properties with great facility, in addition to handling complex geometry. Their efforts led to the development of an integral method which is now widely known as the Finite Element Method (FEM). As can be seen from Figs. 2c and 2d, one of the differences between the IFDM and FEM is that in the former the subdomain is explicitly defined and in the latter, it is a weighted fraction of a larger domain made up of triangles.

Although the early FEM equations were developed from physical considerations (Winslow, 1966; Wilson, 1968), later workers have developed FEM equations using a variety of mathematical techniques such as variational principles (Javandel and Witherspoon, 1968), the Galerkin Method (Zienkiewicz and Parekh, 1970; Pinder and Frind, 1972; Neuman, 1973b) or by the Method of Weighted Residuals (Finlayson, 1972). It was pointed out by Finlayson and Scriven (1967) that from a computational viewpoint the Galerkin approach forms the most direct method of formulating the FEM equations. The Galerkin procedure, which is a type of the weighted residual method, essentially consists of the following.

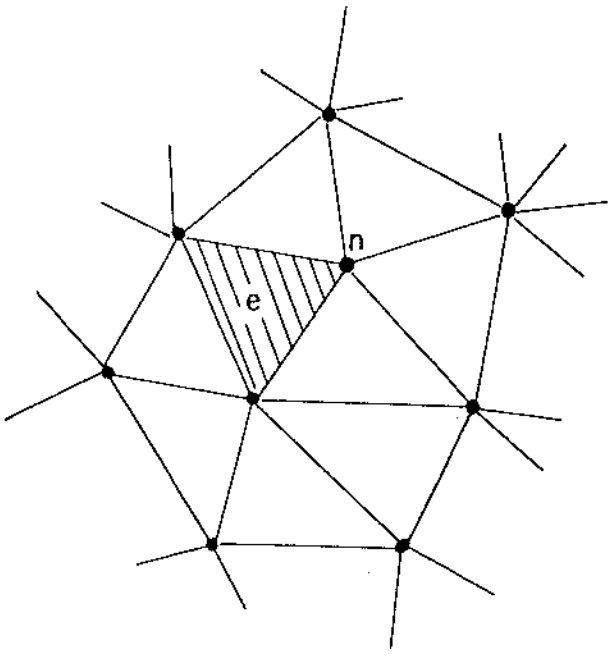

XBL 764-2823

Fig. 3. Discretization of flow region into a system of finite elements, e.

The flow region is first discretized into a system of triangles as in Fig. 3. More general shapes such as quadrilaterals can be used with equal ease, and we are considering triangles only for simplicity. Within the flow region let the dependent variable h vary by the linear relation

$$h \simeq h' = \xi_m(x_i)h_m(t), \qquad \begin{matrix} m = 1,2,3, \ \ldots \ N \\ i = 1,2,3 \end{matrix} \tag{39}$$

where the repetition of the subscript m implies summation. The function $\xi_m(x_i)$ is called a basis function, defined in such a way that $\xi_m(x_i) = 1$ at nodal point m and zero at all other nodal points. The quantities $h_m(t)$ are undetermined coefficients. In the case of the triangular elements of Fig. 3, ξ_m varies linearly over all the elements which ha have m as a corner point. We now substitute (39) for ψ into (31), multiply the PDE by the weighting function ξ_n (the Galerkin weighting function) and integrate over the entire flow region to obtain (Pinder and Frind, 1972)

$$\sum_e \int_{V^e} \xi_n \left[\nabla \cdot \underline{\underline{K}} \nabla \xi_m h_m - m_c \frac{\partial \xi_m h_m}{\partial t} \right] dV = 0 \tag{40}$$

$$n = 1,2,3 \ \ldots \ N \ .$$

Equation 40 implies that there are N basis functions and it has been shown by Forray (1968) that $N \to \infty$, $h' \to h$. Next, Green's first identity (Sokolnikoff and Redheffer, 1966) is applied to (40) to eliminate the second derivative and (40) reduces to

$$\sum_e \left[\int_{V^e} \nabla \xi_n \cdot \underline{\underline{K}} \nabla \xi_m h_m dV + \int_{V^e} m_c \xi_n \xi_m \frac{\partial h_m}{\partial t} dV - \int_{\Gamma^e} \xi_n K \nabla \xi_m h_m \cdot \vec{n} d\Gamma \right] = 0 \ . \tag{41}$$

The surface integral in (41) is nonzero only when the surface of integration coincides with the external surface of the flow region, and then it is prescribed and known. The task of the FEM is therefore to evaluate the two volume integrals in (41).

Although the general form of the Galerkin formulation is well established, some workers (e.g. Neuman, 1973b) have found that the substitution of $h' \simeq \xi_m h_m$ into the time derivative in (40), which gives rise to the so-called consistent mass matrix (Fujii, 1973), may lead to difficulties of convergence or oscillatory solutions. Fujii (1973) has shown on theoretical grounds that under certain conditions, the numerical solution of (41) can violate the Maximum Principle, which states that in the absence of sources or sinks, the maximum potential can occur at the initial time or on the boundary. Narasimhan (1976) found that the numerical solution of (41) may not assure local mass balance although global mass balance may still be preserved. For these reasons, Neuman and Narasimhan (1976) restrict the application of the approximation (39) strictly to the space domain (which gives rise to the so-called lumped mass matrix) and write

$$\sum_e \left[\int_{V^e} \nabla \xi_n \cdot \underline{\underline{K}} \nabla \xi_m h_m dV + \int_{V^e} m_c \xi_n \frac{\partial h^N}{\partial t} dV \int_{\Gamma^e} \xi_n \underline{\underline{K}} \nabla \xi_m \psi_m \cdot nd \right] = 0 \ . \tag{42}$$

in which h^N is the mean value of potential over the subdomain associated with nodal point n.

At this point it is appropriate to outline some of the special advantages of the FEM. By introducing a surface $h = \xi_m h_m$ for the variation of potential over an elemental region, the FEM achieves a general and powerful method of evaluating gradients, which results in three important advantages: (a) it is very convenient in handling arbitrary tensorial quantities such as stress, anisotropy, and dispersion; (b) it is possible to fit higher-order surfaces to the variation of potentials over an elemental region, thereby greatly enhancing the accuracy of evaluating spacial derivatives; and (c) it is possible to approximate complex geometries efficiently by appropriate choice of elemental blocks.

The concept of isoparametric elements is a powerful recent extension of the FEM (Zienkiewicz, 1971; Ergatoudis et al., 1968; Pinder and Frind, 1972). Note that the spatial function $\xi_n(x_i)$ is sufficiently general in nature as to admit of first, second or higher degree algebraic functions. Isoparametric elements are constructed by letting ξ_n be an appropriate higher-order form and making use of curvilinear coordinate transformations. The remarkable feature of the isoparametric elements is that the higher-order approximation not only defines the spatial variation of the dependent variable more accurately, but also enables the handling of curved geometries. In two dimensions, isoparametric elements are curvilinear quadrilaterals, while in three dimensions they may be curvilinear parallelipeds. Isoparametric elements may be quadratic or cubic, depending on whether ξ_n is of second or third degree. The nature of the isoparametric elements is such that a higher-order element need not necessarily be more accurate than a lower-order element (Emery and Carson, 1971). Superparametric and subparametric elements are sometimes used when the variation of potential and the boundary shapes of the elements are to be approximated to different orders of accuracy. Some workers, especially in the field of petroleum engineering, tend to use the power of (39) only for achieving a higher-order approximation for the spatial variation of potential and not for handling curvilinear boundaries. In this approach, the higher-order approximations are used in conjunction with an orthogonal, rectangular grid of mesh points.

It was mentioned earlier that the IFDM is based on surface integration, while the FEM is based on the evaluation of volume integrals. In the case of the simple triangular elements shown in Fig. 3, the equivalence between volume integration and surface integration can easily be recognized (Narasimhan, 1975), leading to an understanding of the conceptual similarities between the two schemes. When the higher-order isoparametric elements are employed, the FEM makes use of selected quadrature points within the element at which the integrals are numerically evaluated.

The Equation Matrices

In the previous section it was shown that the governing equations for the FDM and the IFDM are given by (31) and (29), respectively. The FEM, on the other hand, lends itself to two forms: a consistent mass matrix form (44) as well as a lumped mass matrix form (43). Of these, (31), (29) and (42) all lead to a matrix (Type 1), while (41) leads to a nondiagonal fluid mass capacity matrix (Type 2). These two systems of equations may be written:

$$\underline{\text{Type 1}} \qquad [\underline{A}]\{h\} + [\underline{D}^*]\{\dot{h}\} = \{Q\} \tag{43}$$

$$\underline{\text{Type 2}} \qquad [\underline{A}]\{h\} + [\underline{D}]\{\dot{h}\} = \{Q\} \quad . \tag{44}$$

Each row in the above systems of equations represents the evaluation of mass balance for one nodal point of interest in the system. The matrix $[\underline{A}]$ is a conductance matrix (or "stiffness" matrix as it is often called), which summarizes the coefficients determining mass transfer between connected mass balance subdomains. It is a symmetric, sparse, and usually diagonal matrix. $[\underline{D}^*]$ and $[\underline{D}]$ are matrices of fluid mass capacity, with the asterisk in (43) denoting the fact that the nondiagonal terms in the matrix are zero and $\{Q\}$ is a vector of known source terms. An examination of (44) will also show that the mass balance equation for a given nodal point (a certain row in the system) also contains the time derivatives of the neighboring nodal points, while in (43) the evaluation of mass balance for a given nodal point contains only its own time derivative. As a consequence, (44) not only requires more computer storage but also involves more computational operations. Note that the various methods (FDM, IFDM, FEM) differ primarily in the techniques employed in assembling the various components of the matrices, and it is these techniques which endow the different methods with their special advantages for selected situations.

So far, the comparisons between the different methods have been made on conceptual grounds. In a recent work Wang and Anderson (1976) examined the algebraic equations for the Laplace equation derived for FDM and FEM and found that in several cases, the same set of algebraic equations are generated in more than one way and that the choice of the element shape and basis functions in the FEM is analogous to the choice of integration rule in the FDM.

Once the appropriate system of equations (43) or (44) is chosen, the solution strategy is to choose an appropriate time interval Δt, solve for $\{h\}$ using the known initial condition at t_o, advance to the next time level $t_o + \Delta t$, and repeat the process once again. Note that since h changes continuously during Δt, it is necessary to use appropriate mean values of $\{\bar{h}\} = \{h\}$ in the systems of equations before a solution can be attempted.

Substitution of $\{h\} = \{h^\circ\}$ (where the superscript $^\circ$ denotes the known initial values) in (43) leads to a set of equations in which all quantities are known except the unknown time derivatives $\{\dot{h}\}$, which can now be computed explicitly. These equations are summarized by Equations 1, 2, and 3 in Table I. On the other hand, no such explicit computations are possible in the case of (44) in which the time derivatives of neighboring nodes are part of the mass balance equation for a given

Table I. Summary of Numerical Equations

Explicit Formulations

Equation

(1) FDM

$$G_{i,j} + \frac{1}{(\Delta x)^2}\left[\bar{K}_{i-1,j}(h^{\circ}_{i-1,j} - h^{\circ}_{i,j}) + \bar{K}_{i,j}(h^{\circ}_{i+1,j} - h^{\circ}_{i,j}) + \frac{1}{(\Delta y)^2}\left[\bar{K}_{i,j-1}(h^{\circ}_{i,j-1} - h^{\circ}_{i,j}) + \bar{K}_{i,j}(h^{\circ}_{i,j+1} - h^{\circ}_{i,j})\right]\right] = m_{c,i,j}\frac{\Delta h_{i,j}}{\Delta t}$$

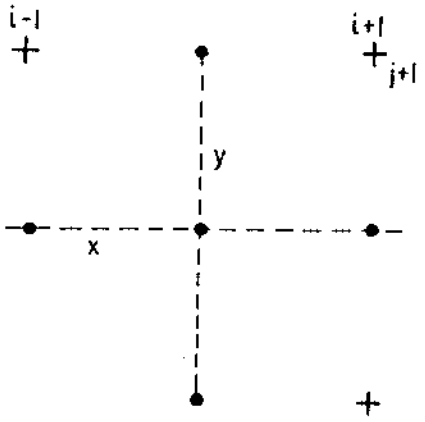

(2) IFDM

$$V_n G_n + \sum_m \frac{\bar{K}_{n,m} A_{n,m}}{D_{n,m}}(h^{\circ}_m - h^{\circ}_n) = M_{c,n}\frac{\Delta h_n}{\Delta t}$$

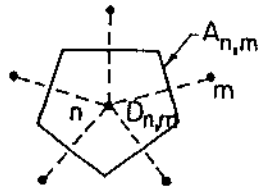

(3) FEM

$$\sum_e \left\{ G_n \int_{V^e} \xi_n dV - \int_{V^e} \Delta\xi_n \cdot \underline{\underline{K}} \Delta\xi_m h_m dV \right\} \left\{ \sum_e m_{c,e} \int_{V^e} \xi_n dV \right\} \frac{\Delta h_n}{\Delta t}$$

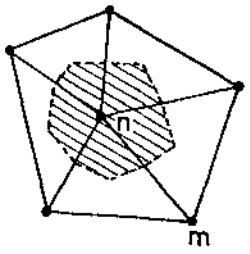

Non-explicit Formulation

(Consistent Mass Matrix)

(4) FEM

$$\sum_e \left\{ G_n \int_{V^e} \xi_n dV - \int_{V^e} \Delta\xi_n \underline{\underline{K}} \Delta\xi_m \cdot h_m dV \right\} = \left\{ \sum_e m_{c,e} \int_{V^e} \xi_n \xi_n \, dV \right\} \frac{\Delta h_n}{\Delta t} + \left\{ \sum_e m_{c,e} \left[\int_{V^e} \xi_n \xi_m \, dV \right] \right\} \frac{\Delta h_m}{\Delta t}$$

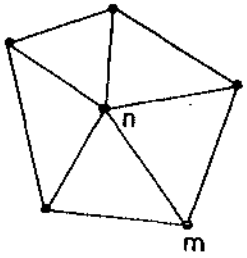

10.	Emsellem and deMarsily (1971)	Inverse Modeling of Alluvial Aquifer North of Strasbourg, France

On the basis of the parallel pattern of water divides and valleys in parts of Central Alberta (Fig. 4), and on the basis of inferred differences in permeability contrasts between geologic formations of the area, Toth (1962) considered individual, small drainage basins to be separate units of the groundwater flow regime. If one assumes that the phreatic surface is fixed and known, then the distribution of hydraulic head in the basin can be found by solving the Laplace equation under appropriate boundary conditions. Using the technique of separation of variables, Toth generated the two-dimensional profile shown in Fig. 5 that shows the division of flow across two adjacent valley sides. Simulations such as these helped Toth to recognize that in a typical groundwater basin one could mathematically distinguish between recharge areas (regions of predominantly downward groundwater motion) and discharge areas (regions of predominantly upward groundwater motion), separated by a median line. He also demonstrated how an uneven physiography or heterogeneity of material properties could lead to subgroundwater systems on different scales (local, intermediate, and regional) in a single groundwater basin.

Perhaps the most important contribution of Toth's investigation was that it provided a formal framework for defining a groundwater basin and its anatomy. Such a framework is of vital interest not only in studying the movement of groundwater but also in interpreting the evolution of the geochemistry of groundwater (Chebotarev, 1955; Davis et al., 1959; Back, 1966).

Freeze and Witherspoon (1968) chose to use the finite difference approach of solving the Laplace equation and were thereby able to simulate far more complex basins than those simulated by Toth. In validating their numerical model, Freeze and Witherspoon modeled the two-dimensional steady-state flow pattern in the Gravelbourg aquifer, Saskatchewan, Canada, the hydrogeology of which had been extensively studied earlier. The results of their simulation are shown in Fig. 6. Their model not only considered the permeability contrasts between various units but also took into account a 20-to-1 anisotropy in certain layers. As can be seen from Fig. 6, the model was successful in simulating the hydrodynamics of the natural system with reasonable accuracy and effort. In an earlier work Freeze (1967) applied the finite-difference approach to simulate a three-dimensional field example as shown in Fig. 7.

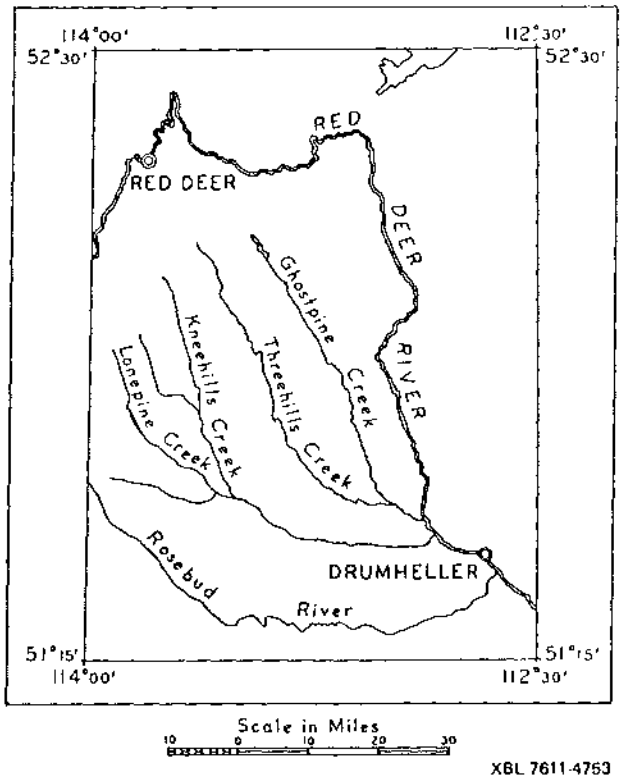

Fig. 4. Parallelism of creeks in Central Alberta (Toth, 1962).

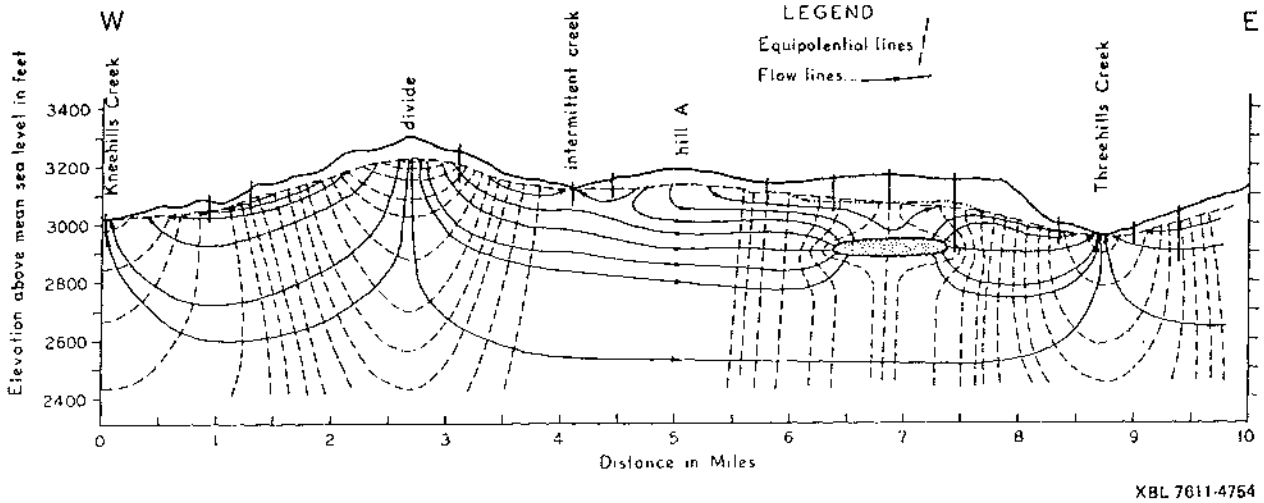

Fig. 5. Steady-state flow pattern, a local flow system, and the effect of a highly permeable body across two adjacent valley sides in Central Alberta, Canada (Toth, 1962).

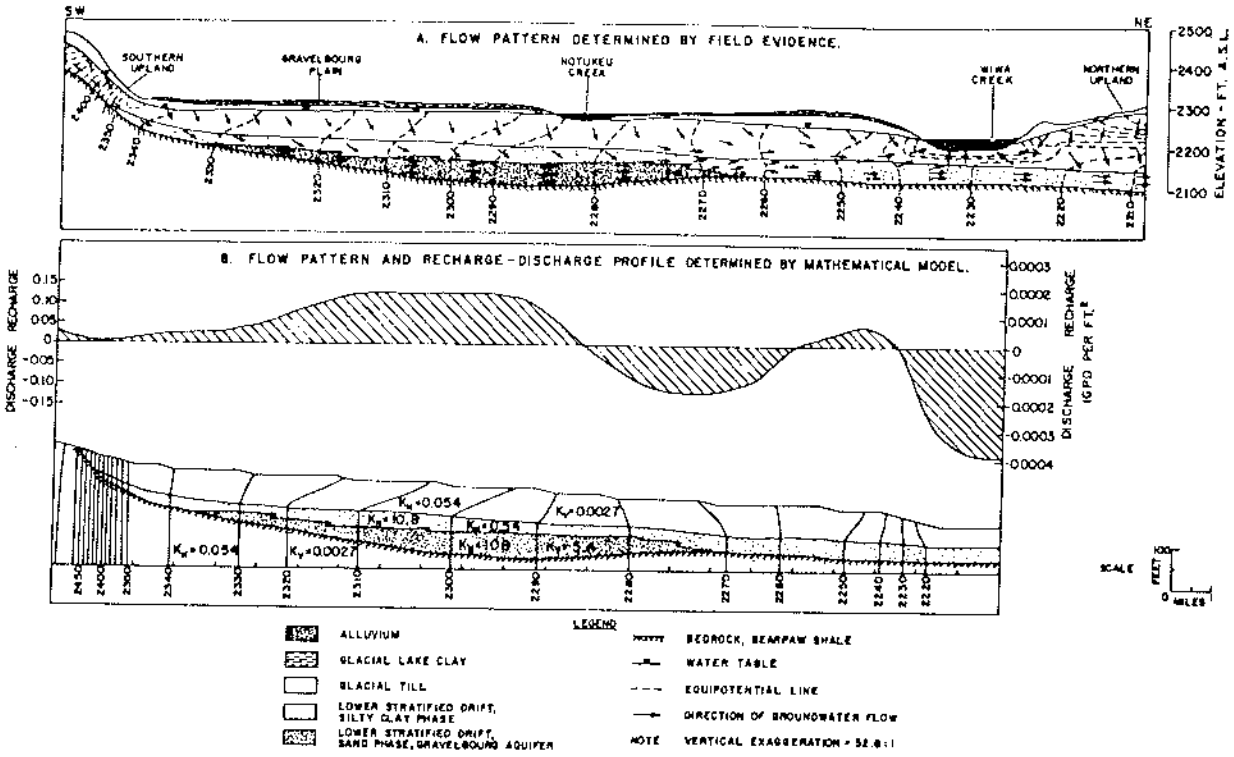

XBL 7611-4755

Fig. 6. Steady-state flow pattern in the Gravelbourg aquifer, Saskatchewan, Canada: comparison of mathematical model with field data (Freeze and Witherspoon, 1968).

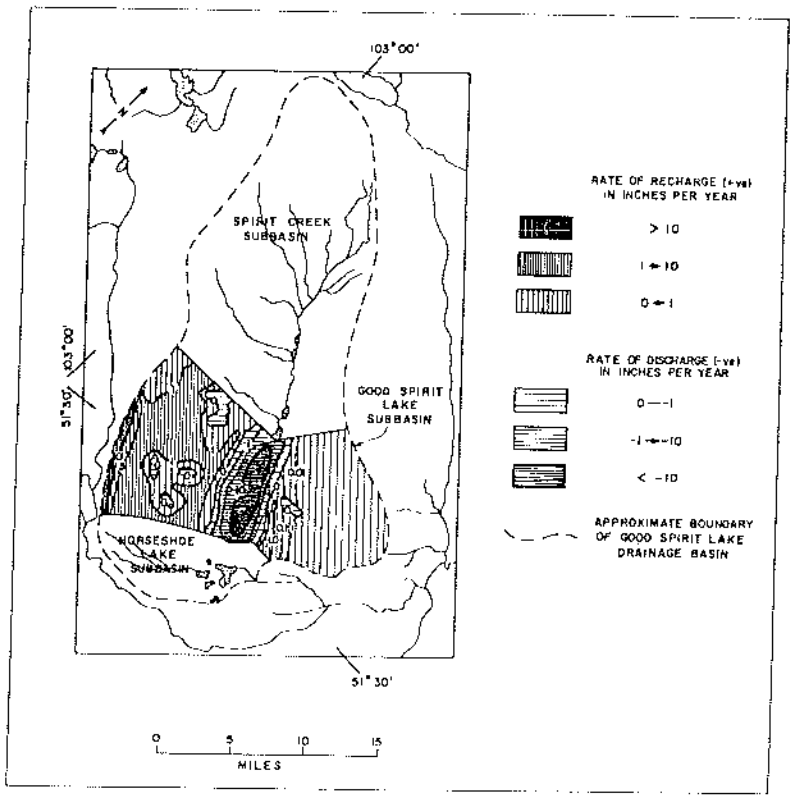

XBL 7611-4756

Fig. 7. A recharge-discharge map from a three-dimensional field example, Good Spirit Lake drainage basin, Saskatchewan, Canada (Freeze and Witherspoon, 1968).

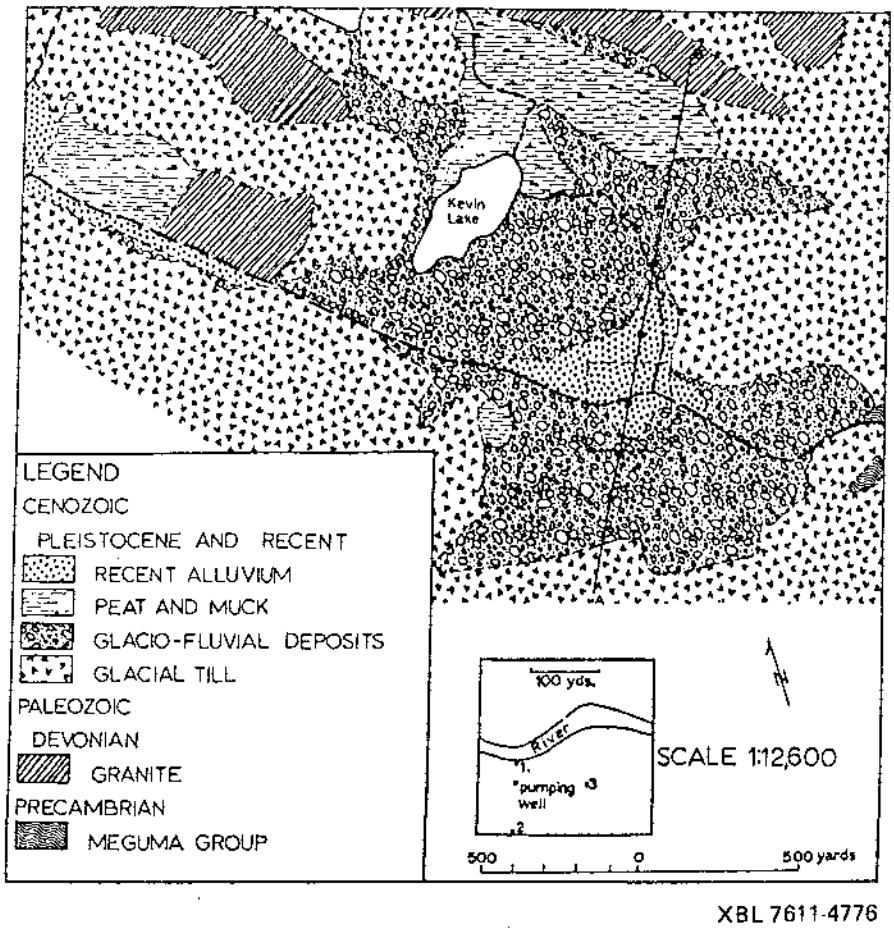

Fig. 8. Geologic map of Musquodoboit Harbour area, Nova Scotia, Canada (Pinder and Bredehoeft, 1968).

While Freeze and Witherspoon (1968) restricted their analysis to the steady-state situation, Pinder and Bredehoeft (1968) developed an implicit finite-difference model for simulating the dynamics of flow in a groundwater basin. They applied their model in evaluating the adequacy of an aquifer at the village of Musquodoboit Harbour, Nova Scotia, Canada (Fig. 8) as a source of water supply. As a first step in their investigation, Pinder and Bredehoeft had to estimate the distribution of aquifer parameters. To this end, they progressively modified the distribution of the parameters in the digital model until the model accurately simulated known pump-test data. Using the modified transmissibility matrix (Fig. 9), they went on to simulate the effects of a production well continuously producing at a rate of 0.963 cfs. (Fig. 10). The simulation led them to conclude that the aquifer would provide an adequate water supply to the village of Musquodoboit. As a check on the digital model, an electrical analog of the aquifer was also constructed and favorable comparisons were obtained between the two models.

Prickett and Lonnquist (1971) applied the finite-difference technique to model the Cambrian-Ordovician aquifer in northeastern Illinois. This case history is of considerable interest in that the spatial as well as the temporal scales chosen for modeling are very large. The model was used to simulate an area of approximately 24,000 square miles over a time period of 130 years.

The Cambrian-Ordovician aquifer, which is about 1000 ft thick, can be vertically divided into 4 hydraulically connected subunits, with the transmissivity decreasing from about 17,000 gdp/ft towards the top to almost zer towardsthe bottom (Fig. 11). The aquifer is under leaky artesian conditions and, in the northern parts of the simulated area, receives small quantities of recharge from the younger Silurian rocks or glacial drift through intervening shale formations of relatively low permeability.

The Cambrian-Ordovician aquifer has been under intensive development since 1864 and the withdrawal has increased from about 200,000 gpd in 1864 to about 52,4 million gpd in 1960. Due to heavy pumpage, the piezometric surface had declined by as much as 600 ft in some parts of northeastern Illinois (Fig. 12). This excessive drawdown in the piezometric head has now converted the artesian aquifer to water-table conditions in some parts of the Chicago region.

The purpose of the Prickett-Lonnquist model was to predict the response of the Cambrian-Ordovician aquifer over a 130-year period from 1864-1995, using projected pumpage estimates in-

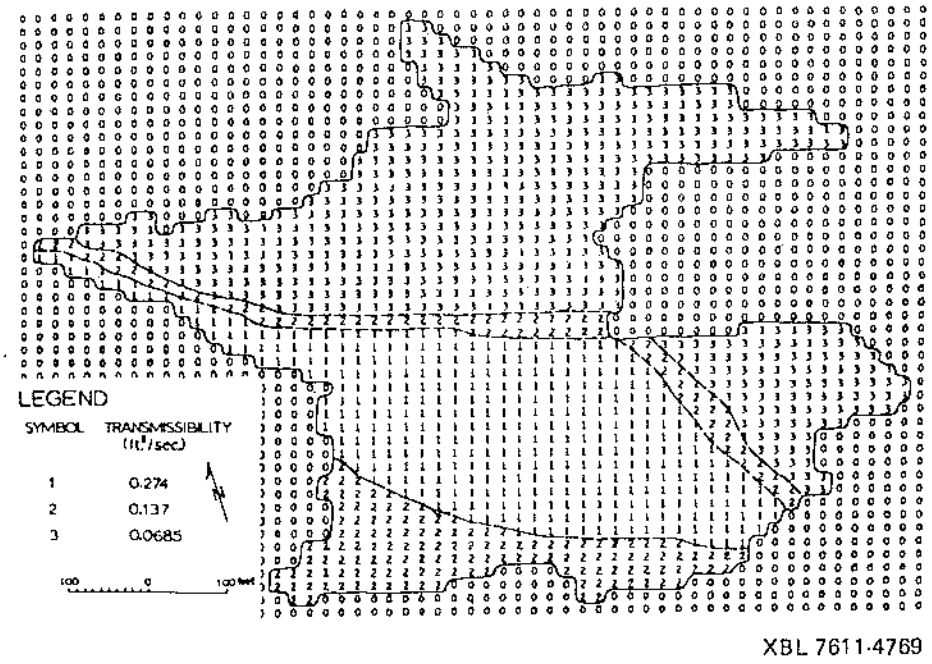

Fig. 9. Modified transmissibility matrix of the Musquodoboit aquifer adjusted on the basis of test-well logs and numerical simulation (Pinder and Bredehoeft, 1968).

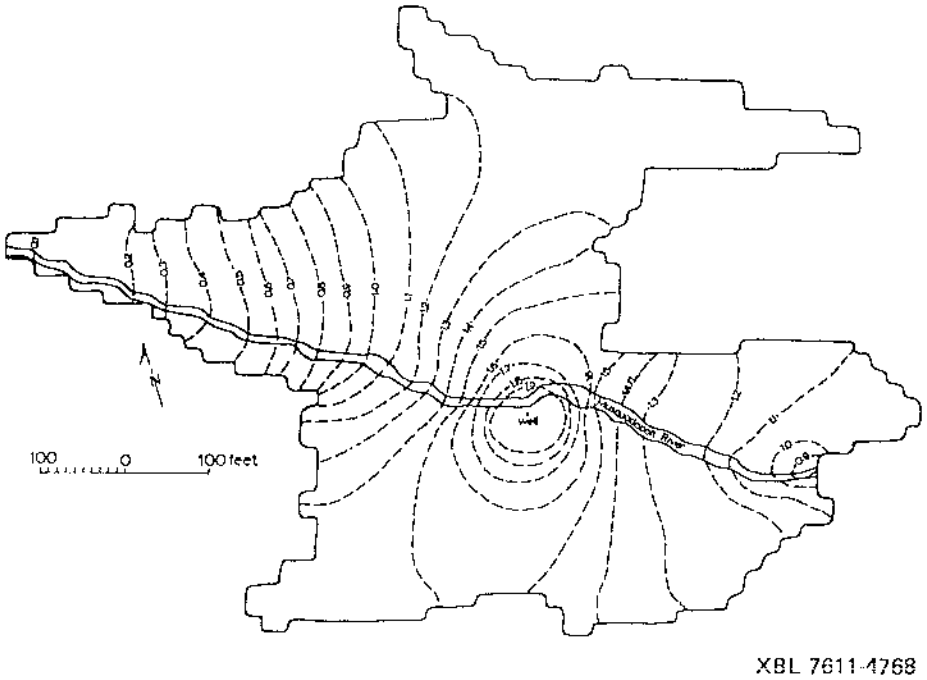

Fig. 10. Piezometric surface after 206.65 days of pumping at 0.963 cfs, as determined by the numerical model (Pinder and Bredehoeft, 1968).

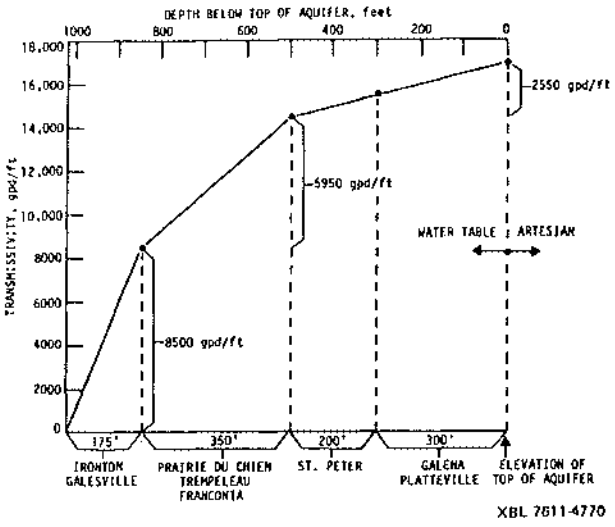

Fig. 11. Transmissivity variation of units of Cambrian-Ordovician aquifer in Chicago region (Prickett and Lonnquist, 1971).

creasing to 145 million gpd in 1995. This model is a nonlinear model in that one can simulate a prescribed variation of pumpage with time (Fig. 13) as well as the decrease in transmissivity as a function of saturated thickness, when the aquifer undergoes dewatering. The artesian coefficient of storage was estimated to be 5×10^{-4}, while a specific storage of 5×10^{-2} ft^{-1} was used for the dewatering aquifer. Reasonable agreement between the model and the observed data for the period 1864-1958 can be seen in Fig. 12. The computed total declines in water level at the end of 1995 are shown in Fig. 14.

The interaction of the shallow groundwater system with surface water bodies through the unsaturated zone is often of interest to engineers concerned with water-balance studies related to watersheds. Stephenson and Freeze (1974) applied the unsaturated-saturated flow finite-difference model of Freeze (1971) to study runoff-generation mechanisms in an experimental watershed in Reynolds Creek, Idaho. Their aim was to simulate transient saturated-unsaturated flow contributions to stream discharge and to use the model as an aid in interpreting field measurements.

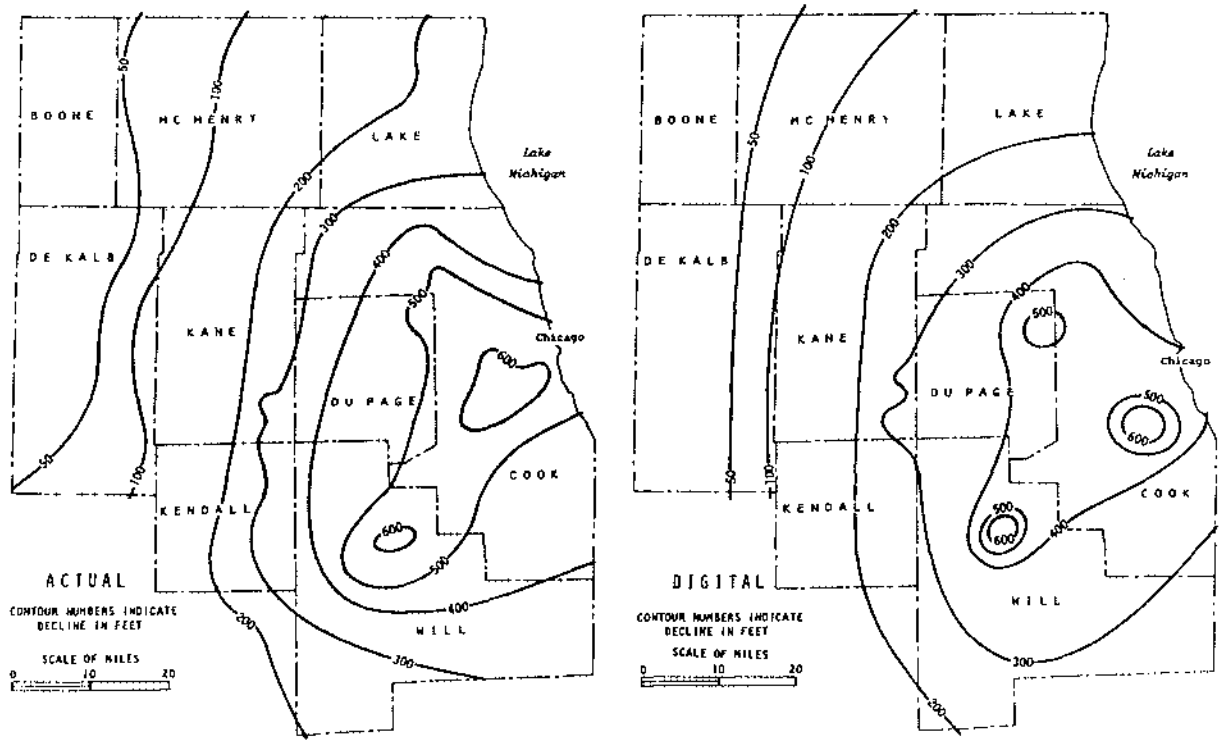

Fig. 12. Piezometric declines in Cambrian-Ordovician aquifer, 1864-1958: comparison of field and numerical results (Prickett and Lonnquist, 1971).

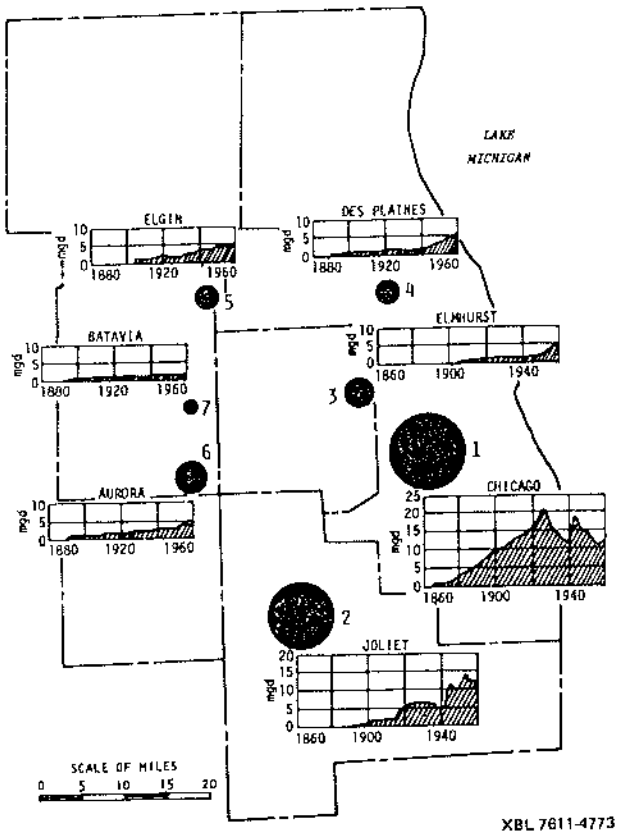

Fig. 13. Pumpage history of the Cambrian-Ordovician aquifer (Prickett and Lonnquist, 1971).

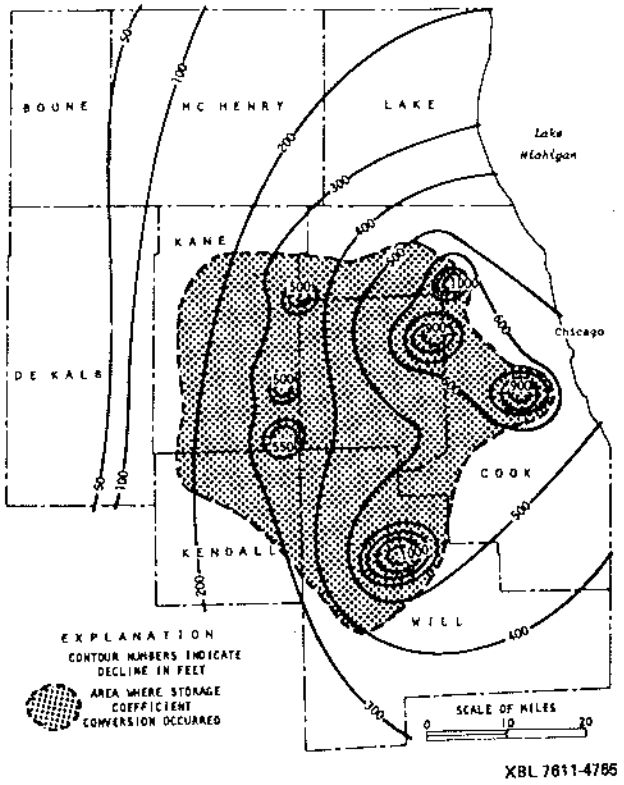

Fig. 14. Computed piezometric declines, 1864-1995, in the Cambrian-Ordovician aquifer (Prickett and Lonnquist, 1971).

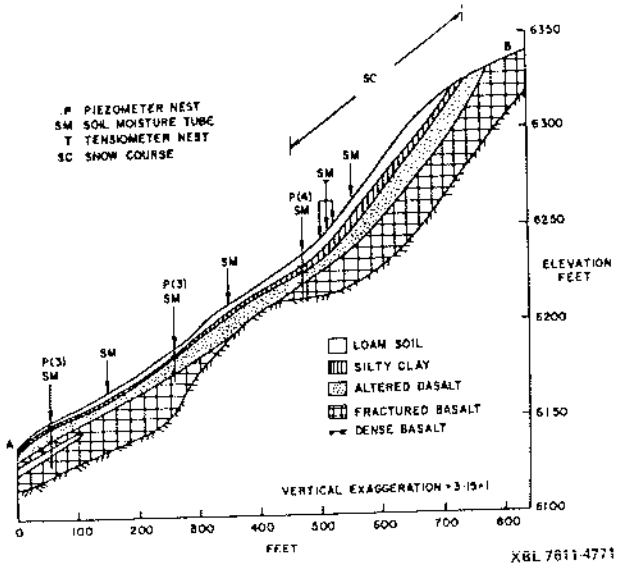

Fig. 15. Geologic cross section across Reynolds Creek, Idaho and guide to instrumentation (Stephenson and Freeze, 1974).

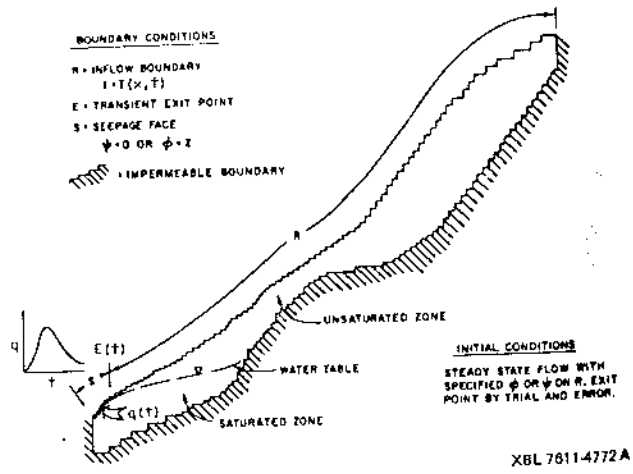

Fig. 16. Boundary and initial conditions, simulation of Reynolds Creek, Idaho (Stephenson and Freeze, 1974).

The geologic profile at the site along with the disposition of field instrumentation is given in Fig. 15. The simulation problem was one of solving the parabolic nonlinear differential equation subject to the initial and boundary conditions shown in Fig. 16. The flow region contained

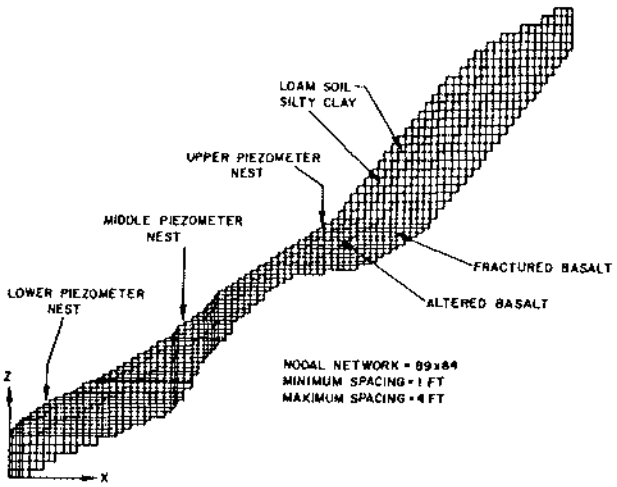

XBL 7611-4767

Fig. 17. Finite difference network for the Reynolds Creek basin, Idaho (Stephenson and Freeze, 1974).

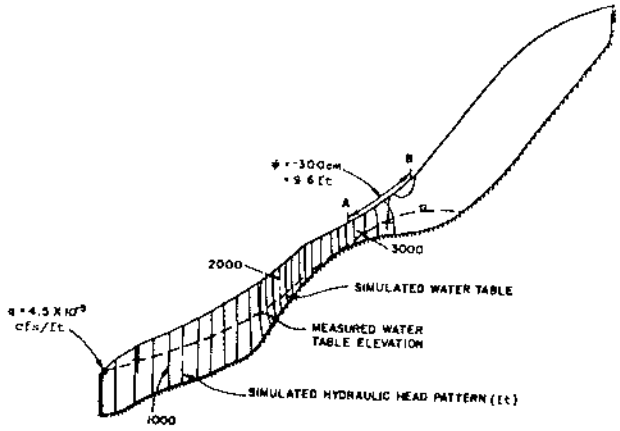

XBL 7611-4763 A

Fig. 18. Calibrated steady-state flow system for April 5, 1971, Reynolds Creek, Idaho (Stephenson and Freeze, 1974).

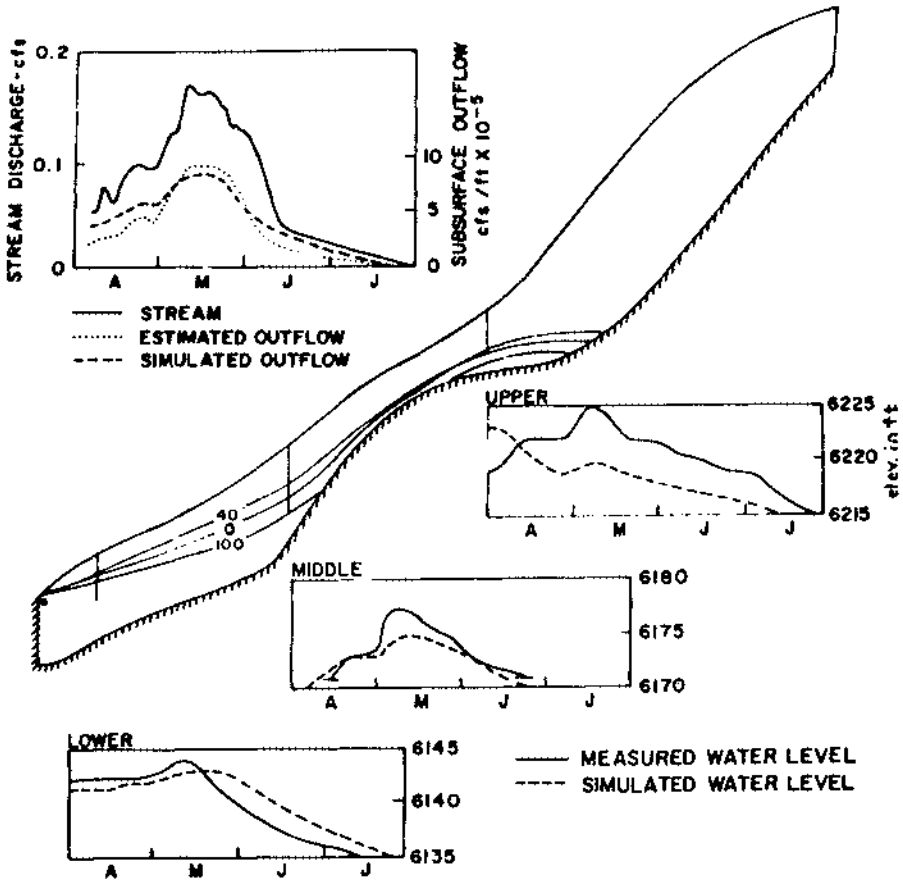

XBL 7611-4766

Fig. 19. Calibrated transient flow system for April 5 to July 13, 1971, Reynolds Creek, Idaho (Stephenson and Freeze, 1974).

three materials (fractured basalt, altered basalt, and soil) with saturated permeabilities varying from 3.8 x 10^{-4} to 15 x 10^{-4} dm/sec. K and varied with in the unsaturated zone, and soil compressibility was neglected due to its relative unimportance in near-surface systems. The finite-difference network used in the simulation is shown in Fig. 17.

The primary task of Stephenson and Freeze was to calibrate the model by adjusting the input parameters and boundary conditions as well as the

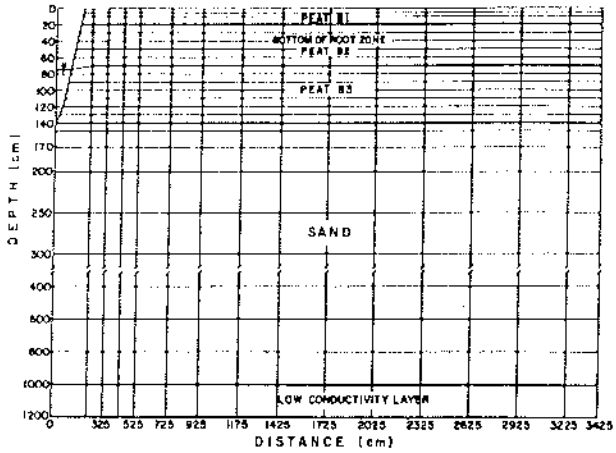

Fig. 20. Finite-element network of layered soil, De Groeve, Netherlands (Feddes et al., 1975).

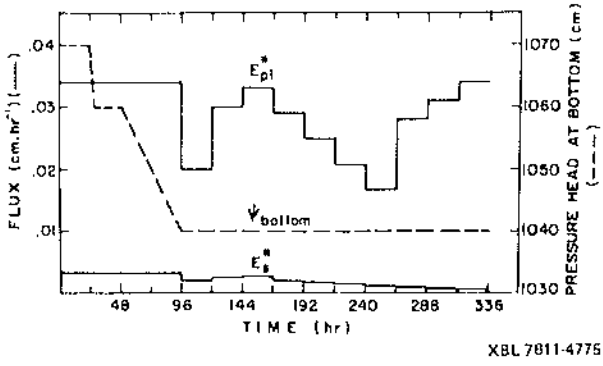

Fig. 21. Time dependence of boundary conditions, De Groeve finite-element simulation (Feddes et al., 1975).

geological configuration, using trial and error methods. The idea was to obtain a good fit with observed field data such as water table elevations, vertical hydraulic gradients at piezometer sites, the stream-flow hydrograph, pressure heads, and moisture contents. The calibrated steady-state system, which formed the initial conditions for the transient model, is shown in Fig. 18. The results of the transient simulation at the end of 100 days are presented in Fig. 19. This transient simulation was also effectively a calibration run, in that the saturated permeabilities of the three formations, as well as the inflow function over the inflow boundary, were adjusted to obtain the best match with field observations.

It can be seen in Fig. 19 that the calibrated model agrees reasonably well with the field observations of subsurface contributions to stream flow and the water levels observed in piezometers. Whether the calibrated model can indeed be considered validated is difficult to assess. For example, if this model can accurately predict the check parameters for a subsequent snowmelt period, one could consider that the model is indeed validated. However, difficulties in obtaining reliable field data on the inflow function across the inflow boundary and the sensitivity of the model response to the inflow function, are bound to thwart such a validation procedure. As the authors themselves point out, the value of this case history lies in the recognition that the principal role of this type of mathematical model is to help define more clearly the various mechanisms within the hydrologic cycle so that simpler hydrologic response models can be more firmly based on reality

An important class of problems related to shallow groundwater systems is that of simulating plant root-soil interactions. Feddes et al. (1975) used the finite-element method to simulate evapotranspiration in an agricultural field in De Groeve, Netherlands. The field in question is covered by peaty soil with an average thickness of about 1.4 m and is underlain by about 10 m of sandy soil. The sandy soil in turn is separated from a deeper aquifer by a 2 m aquitard of clayey soil. The deeper aquifer is intermittently pumped by means of domestic wells outside the area of interest. The field is traversed by several unlined irrigation ditches where water levels can be controlled at will.

Due to symmetry, only one half of the region between two ditches need by considered and a cross section, together with the FEM network, is shown in Fig. 20. The peat and sand layers were assumed to be anisotropic with horizontal permeability ten times the vertical. The root zone is assumed to increase from an initial depth of 40 cm to 50 cm at the end of 168 hours. The water level in the ditch is assumed to be the same as the initial depth of the water table, 74 cm below ground level, and initially the system is assumed to be hydrostatic. The time-dependent hydraulic-head variation in the pumped aquifer as well as the maximum possible rates of soil evaporation and plant transpiration are illustrated in Fig. 21.

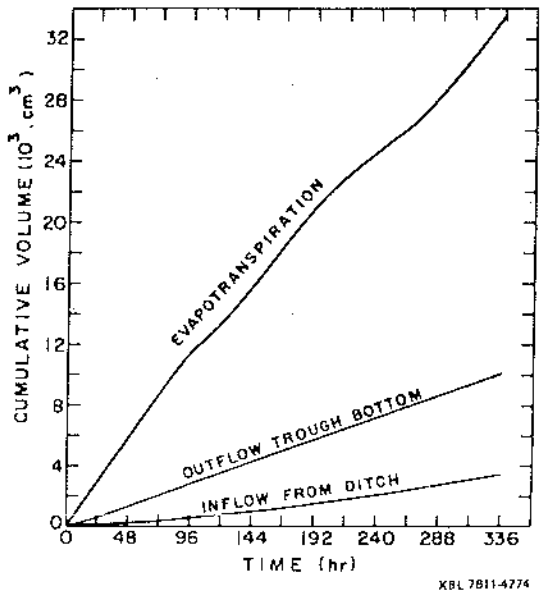

Fig. 22. Computed boundary fluxes, De Groeve finite-element simulation (Feddes et al., 1975).

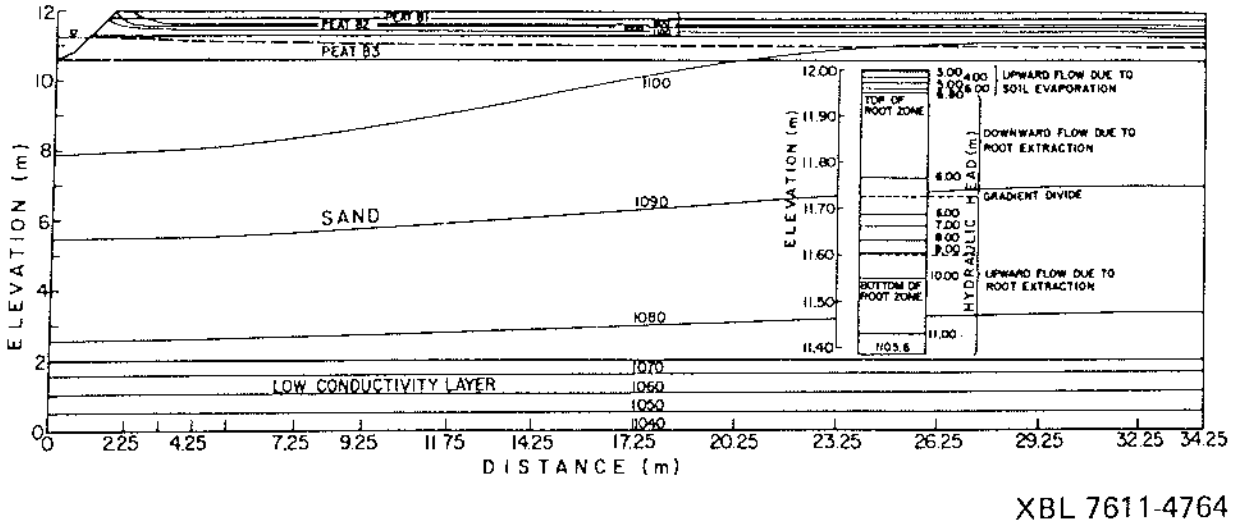

Fig. 23. Distribution of hydraulic head after 336 hours, De Groeve finite-element simulation (Feddes et al., 1975).

The dynamic numerical simulation extended over a period of 335 hours. Time steps varied from an initial value of 1 hour to 48 hours. Figure 22 shows results for the cumulative fluid fluxes leaving or entering the system due to evapotranspiration, ditch infiltration, and leakage to the underlying pumped aquifer. The distribution of hydraulic heads in the system at the end of 336 hours is shown in Fig. 23. The inset in this figure shows how local upward and downward zones of water movement exist in the uppermost part of the system, and are controlled by evaporation and root extraction.

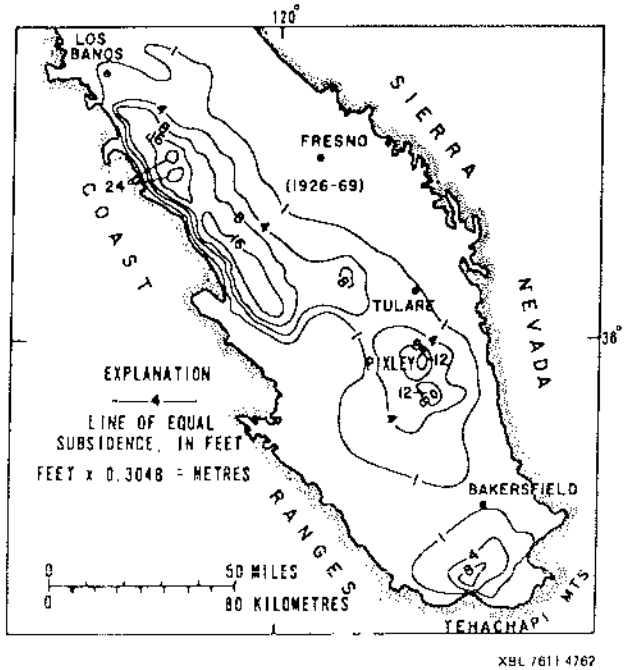

Fig. 24. Extent and magnitude of observed land subsidence, San Joaquin Valley, California (Helm, 1975).

The principal phenomenon of interest in the case histories presented so far has been the movement of water. When hydrogeologists are concerned with the problem of land subsidence due to groundwater extraction, the main phenomenon of interest becomes the movement of the soil skeleton, rather than the movement of water. Helm (1974, 1975) successfully simulated the land subsidence observed at Pixley, California, using the one-dimensional consolidation theory of Terzaghi (1925). The geographic location of the Pixley site and the extent and magnitude of subsidence in the San Joaquin Valley are shown in Fig. 24. The compacting groundwater body at Pixley consists of a sequence of intercalated sands (aquifers) and clays (aquitards) between depths of 355 and 760 ft. Water-level changes in the hydraulically interconnected, highly permeable aquifers are essentially the same and have been systematically observed over two decades by the U.S. Geological Survey. These water-level changes form the boundary conditions controlling drainage (and the consequent compaction) of the aquitards. In addition, since 1959, the compaction of the entire system, down to 760 ft, has been monitored by means of extensometers. The time-dependent changes in water levels (applied stress at the aquitard interface) and the observed compaction are shown in Fig. 25.

In using a finite-difference model, Helm (1975) assumed that almost all the observed compaction was taking place in the clay and that the clay possessed nonreversible compaction properties. The aquitard parameters, which were constant with time were as follows: permeability = 3×10^{-3} ft/year; recoverable specific storage = 4.6×10^{-6} ft^{-1} and nonrecoverable specific storage = 2.3×10^{-4} ft^{-1}. As is obvious from Fig. 25, the simulation problem is one of modeling a cyclic boundary condition in conjunction with nonreversible material properties. A comparison of the observed and computed compaction at Pixley is shown in Fig. 26, and it is seen that the agreement between the two is reasonably good considering the complexity of the real system.

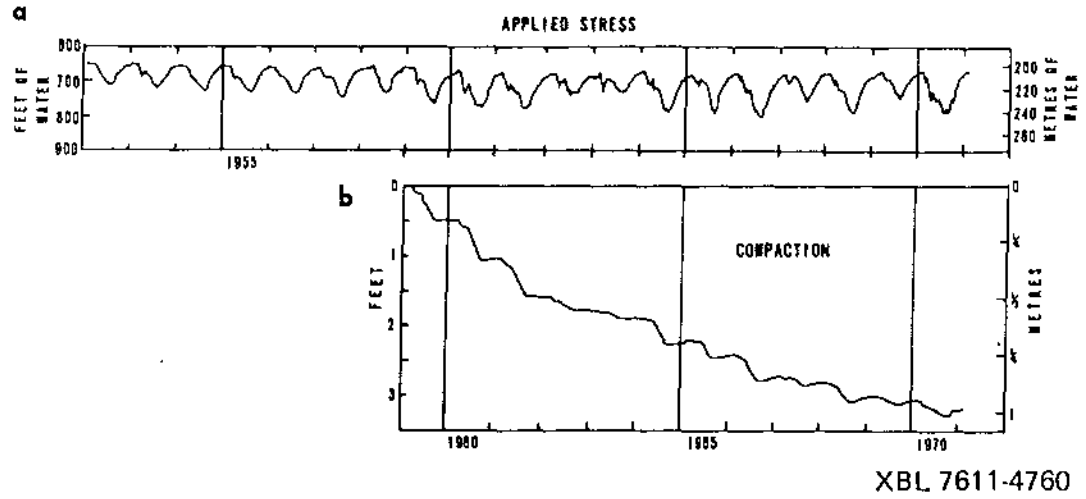

Fig. 25. Field data measured near Pixley, California; a) average applied stress, and b) cumulative compaction (Helm, 1975).

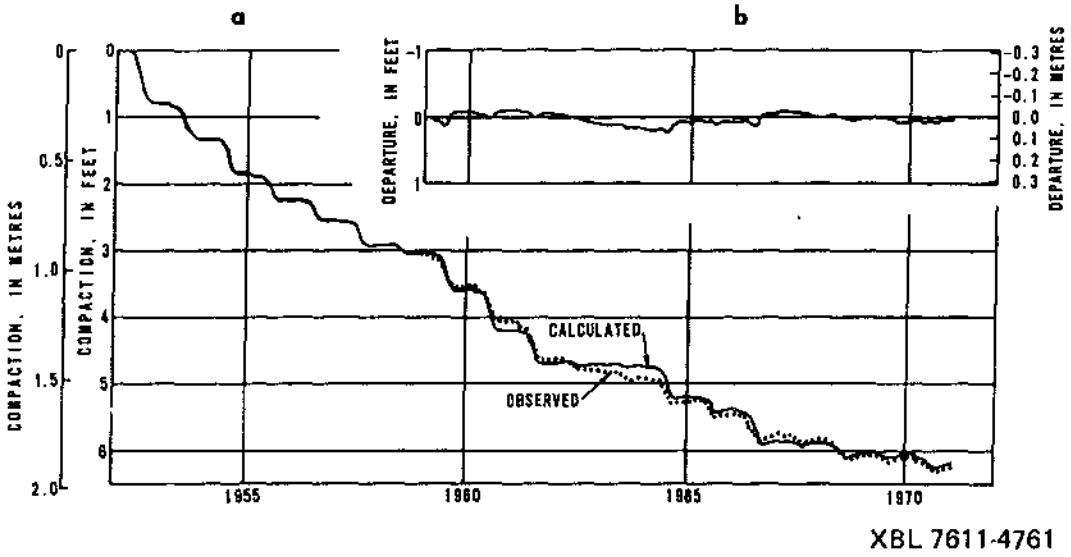

Fig. 26. Comparison of computed and observed compaction at Pixley, California (Helm, 1975).

The historic city of Venice provides another case history for simulating land subsidence (Gambolati and Freeze, 1973; Gambolati et al., 1974). The city has been sinking at an alarming rate (10 cm during 1952-1969) in recent years mainly due to heavy groundwater withdrawals in the Merghera industrial area about 10 km to the west. The purpose of the mathematical simulation was to correlate subsidence and groundwater withdrawal from past data and then to investigate how the adverse effects of ground settlement could be halted by various programs of modified groundwater manage management.

The city of Venice is underlain down to about 330 m by a system of sands and silts with interbedded clays (Fig. 27). Although the material properties of these materials are locally known from laboratory data, their regional properties are not known with any degree of certainty. Due to the sparseness of available field data and the axisymmetric nature of the proposed model, the authors chose to use a dual simulator. This consisted of a finite-element hydrologic model for computing head changes in the aquifers as a function of time and a one-dimensional finite-difference subsidence model for the aquitards, in which the calculated head changes in the aquifers would constitute the boundary conditions. In the hydrologic model, the flow region was divided into a sequence of five aquifers and from intervening aquitards while, in the subsidence model, the vertical column was divided into 20 aquitards. The behavior of the subsidence model is very similar

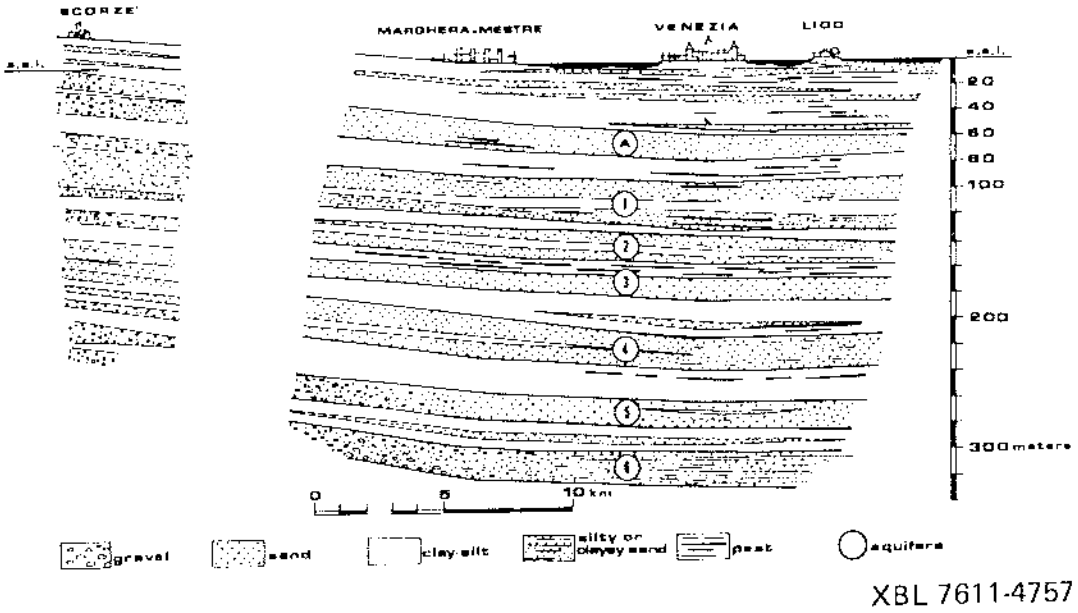

Fig. 27. Geologic cross section from west to east of the Venice lagoon (Gambolati et al., 1974).

to that of Helm (1974, 1975) in using the Terzaghi theory and in providing for nonrecoverable compressibility coefficients.

The first task in the simulation was to calibrate the hydrologic model. The calibration procedure was essentially one of trial and error. The following range of parameters was investigated: for the aquifers, permeability 3.2 x 10^{-3} to 1.6 x 10^{-2} cm/sec, compressibility 1 x 10^{-4} cm^2/kg; for the aquitards, permeability 1 x 10^{-6} to 1.6 x 10^{-5} cm/sec, compressibility 1.5 x 10^{-3} to 3 x 10^{-3} cm^2/kg. A comparison of the computed piezometric head declines in the aquifers and the computed subsidence with the historical records up to 1970 is shown in Figs. 28 and 29. Using these calibrated values, the subsidence in Venice was predicted for several future pumping schedules as shown in Fig. 30. The results of the prediction indicated that if the pumping rates are kept constant at present values, a further 3 cm subsidence could be expected to occur in the future. Subsidence could be arrested by reducing the Marghera withdrawal by 25% along with shutting down pumping of the Tronchetto well. Cessation of all pumping would provide a modest rebound of 2 cm.

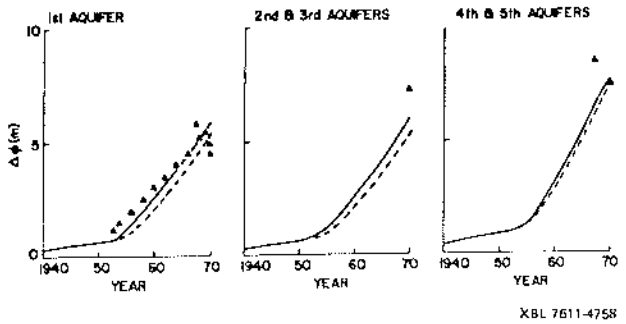

Fig. 28. Comparison of observed and computed piezometric head changes at Venice. Dashed lines represent head changes solely due to Marghera pumping. Triangles represent observed values (Gambolati et al., 1974).

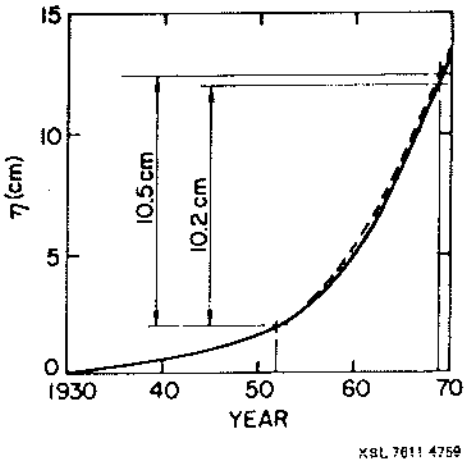

Fig. 29. Computed subsidence at Venice using two different calibration parameters (Gambolati et al., 1974).

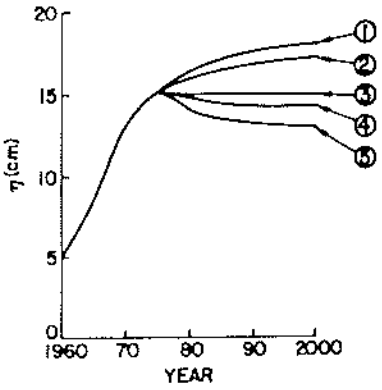

Predicted subsidence in Venice for several future pumping schedules for the VE 2 case.

XBL 765-1712

Fig. 30. Predicted subsidence for Venice for several future pumping schedules (Gambolati et al., 1974).

The next case history to be discussed pertains to the use of statistical techniques to establish the spatial variation of material properties in an alluvial basin with meager borehole data. Lippmann (1973) chose this approach to model the Mocho subbasin of the Livermore Valley, California (Fig. 31). The two-dimensional groundwater system simulated was approximately 10,000 ft long and 200 ft thick and was idealized as comprised of 2 materials: a high-permeability material (material 1) containing sand, gravel, boulder, and associated sediments, and a low-permeability material (material 2) containing clay, sandy clay and other clayey sediments. In all, electrical and lithological data were available from the six boreholes distributed over the system. Because the alluvial sediments have been deposited by meandering streams, correlation of adjacent borehole

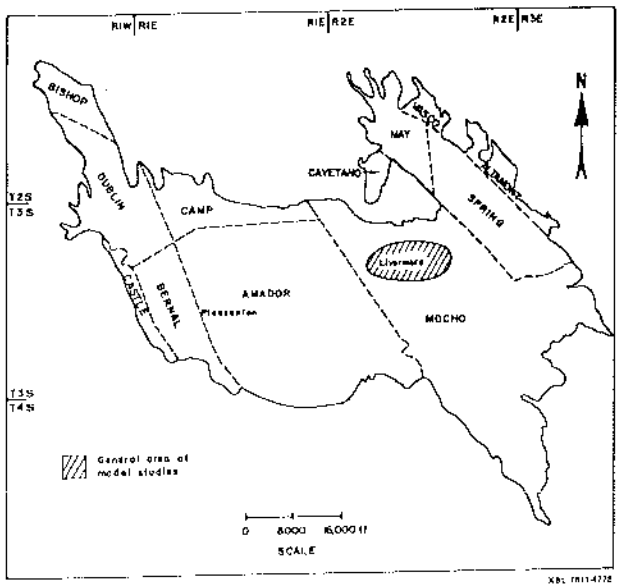

Fig. 31. Groundwater subbasins of the Livermore valley, California (after Lippmann, 1974).

sequences is almost impossible.

In order to achieve a steady-state hydrologic simulation of the basin, Lippmann wanted to compute a statistically equivalent hydraulic conductivity of the system, which, when multiplied by the prevalent hydraulic gradient, would pass the same flux across a unit area as that of the prototype. The calculation of the equivalent hydraulic conductivity was to be done in two steps. The first step was to set up a statistical "Poisson-line" model of the heterogeneous system (Fig. 32) using the probability distribution determined by a Markov chain process of analyzing repetitions at 2-ft intervals as observed in the boreholes. In the second stage, the heterogeneous flow region represented by the Poisson line model was solved for the Laplace equation using simple prescribed boundary conditions.

The FEM analysis for potential consisted in matching different-sized networks to the simulated sections. It was found that as the shapes of the elements were changed from squares to rectangles with elongations as much as 1 x 50, the computed flow rates increased. In the absence of appropriate accuracy estimates for the FEM when applied to complex geometries and strong permeability contrasts, it is obvious that the calculated effective hydraulic conductivity is subject to certain model-induced uncertainties. The results obtained from two different FEM meshes are presented in Table II.

The last case history that we shall consider is the application of the inverse method by Emsellem and DeMarsily (1971) to the estimation of transmissivity distribution in an alluvial aquifer of the Rhine River Valley, north of Strasbourgh, France. In their parameter identification work, Emsellem and DeMarsily use multiple-objective criteria, instead of minimizing a single-error criterion. Their first objective is to minimize a functional of the residual errors (calibration errors) in a direct formulation of the inverse problem. Their second objective is a criterion for the physical plausibility of the possible solutions. The plausibility criterion used by the authors is that the solution remain uniform (or flat) over the entire flow region. Their approach is to gradually decrease the calibration error by relaxing a certain measure of uniformity until the point is reached when further relaxation of this measure does not cause any substantial reduction in the value of the error functional (Neuman, 1975a).

To test the validity of their method, Emsellem and DeMarsily (1971) first computed the transmissivity distribution in the aquifer by the inverse method, using for input data the known steady-state piezometric head distribution over the area of study. Their results are shown in Fig. 33. Using the transmissivity distribution so calculated, they went on to recalculate the steady-state head distribution over the same basin. A comparison of the computed and observed piezometric heads is shown in Fig. 34. The hatching in the figure represents the difference between compu computed and observed values and is thus an indication of the calibration error.

Table II. Results of statistical analysis of data obtained in using 49 x 49 and 16 x 400 finite element meshes.

	Mesh 49 x 49	Mesh 16 x 400
Proportion of Material 1 (p_1)		
Sample mean	0.412	0.412
Sample standard deviation	0.016	0.020
K_E / K_1, expressed in percent		
Sample mean	36.9	20.5
Sample standard deviation	1.74	3.24
Sample correlation coefficient between p_1 and K_E / K_1	0.889	0.775
Flow rate (Q), in gpd/ft		
Sample mean	280	156
Sample standard deviation	13.1	24.6

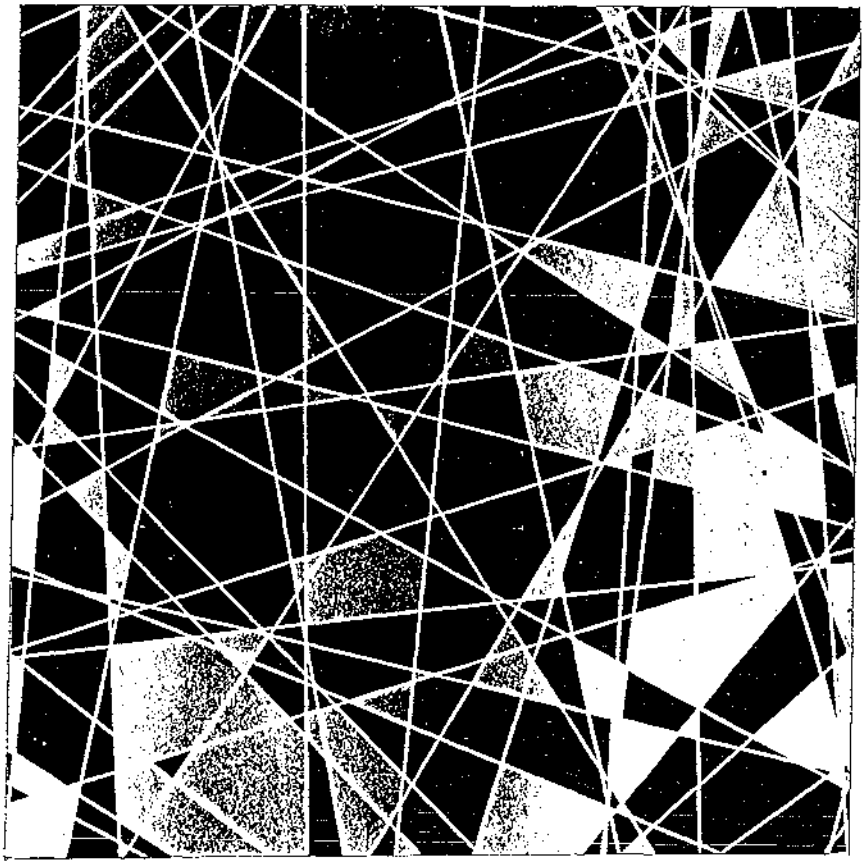

XBL 768-6902

Fig. 32. Example of a Poisson-line model with material no. 1 shaded (Lippmann, 1973).

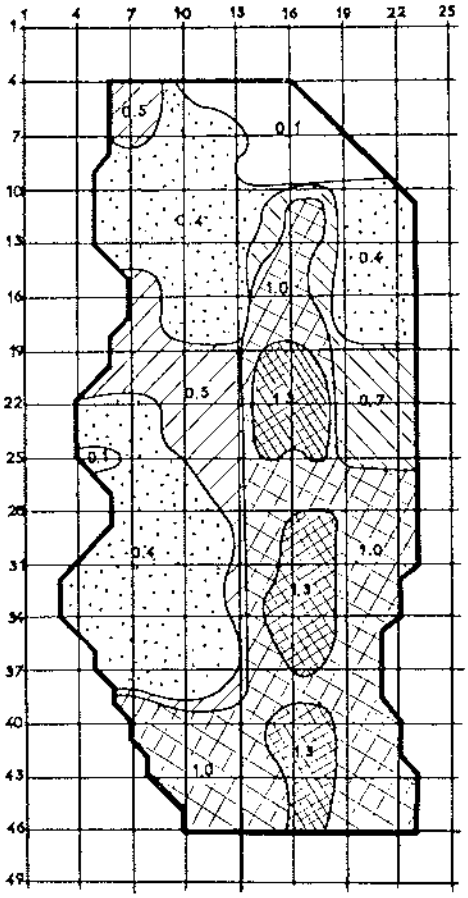

Fig. 33. Distribution of transmissivity over the Rhine aquifer north of Strasbourg, France, computed by the inverse method (Emsellem and de Marsily, 1971).

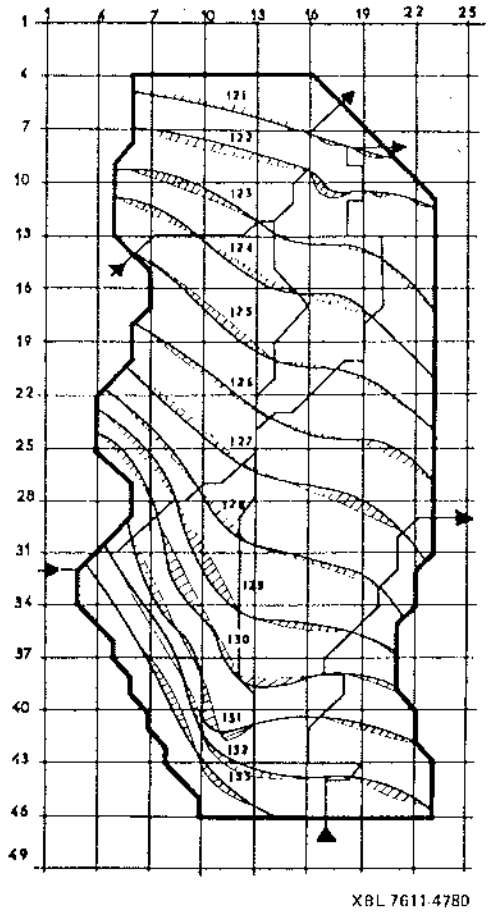

Fig. 34. Rhine aquifer, north of Strasbourg, France: comparison of observed heads with those computed using the transmissivity values determined by the inverse method. Shaded area is the difference between the two values (Emsellem and de Marsily, 1971).

CONCLUDING REMARKS

From the survey carried out in this paper, there is little doubt that numerical modeling is now established as a very valuable tool in understanding groundwater systems. The classical finite-difference approach continues to enjoy wide popularity due to its simplicity and its easy extension to nonlinear as well as multidimensional problems. The more recent finite-element method is a powerful technique in handling complex geometry and arbitrary tensorial quantities as well as providing the option of higher-order approximations for the dependent variable in space and time. Due to limitations of computer storage and computational effort, some difficulties exist in applying the FEM to three-dimensional and nonlinear problems.

In considering the future for numerical modeling of regional groundwater systems, the primary question concerns the degree of applicability to actual field situations. It is apparent that the models are most useful when employed in a deterministic manner to synthesize material properties and geometry and to predict the time-dependent response of a given system. Unfortunately, there are some limitations to such applications. First, the material properties as applied to porous media are macroscopic averages. These averages, combined with the heterogeneity of grain-size distribution in natural sediments, are fundamentally statistical in nature and therefore can not really be represented by deterministic values. Secondly, the sparsity of samples introduces a statistical element in the parameters used in the regional model. It is quite apparent that laboratory measurements and other small-scale experiments used for parameter estimation are inadequate for arriving at the distribution of material properties over the global system.

There is thus a significant trend in attempting to apply inverse methods of parameter estimation and this trend will definitely be pursued in the future. The trial and error methods of parameter estimation used in many of the case histories described here constitute the intuitive and simple approach to the inverse problems. The more sophisticated techniques of linear and quadratic programming seek to achieve a more rational and efficient method of model parameter estimation. Much continued activity in the use and improvement of these techniques can be expected in the future.

It should be remembered that the process of obtaining a solution to a parameter estimation problem actually consists of choosing a most plausible solution from a class of non-unique solutions. In order that a most reasonable choice be made, it is imperative that a good knowledge of the geologic makeup of the field system is forthcoming. Thus, the mathematical model in itself does not constitute an effective tool of analysis unless it complements field observations.

Apart from the ability of predicting the response of real systems to various plausible input functions, and of identifying system parameters, numerical models have a very special and very powerful advantage. This results from the fact that by simulating various hypothetical situations numerically, one should be able to more clearly define the actual mechanisms that control a given complex field situation.

Until now, mathematical models have been employed principally for predicting groundwater flow patterns and, to a lesser extent, for parameter estimation. The power of the models, however, has not been utilized to study problems related to the important aspects of groundwater prospecting, design of data collection networks and instrumentation. There is little doubt that numerical models have a lot to offer in regard to understanding these areas of hydrogeology.

NOMENCLATURE

$[\underline{A}]$	conductance or "stiffness" matrix	
a	a matrix-fracture coefficient	[1]
C	specific moisture capacity	[1/L]
C_c	compression index	[1]
C_s	swelling index	[1]
D	soil moisture diffusivity	$[L^2/T]$
$D_{n,m}$	distance between nodal points n and m	[L]
$[\underline{D}]$	nondiagonal capacity matrix	
$[\underline{D}^*]$	diagonal capacity matric	
e	void ratio	[1]
E	potential evaporation	$[L^3/T]$
E*	potential evapotranspiration	$[L^3/T]$
g	gravitational constant	$[L/T^2]$
G	volumetric rate of fluid generation per unit volume	$[L^3/L^3T]$
h	hydraulic head	[L]
h'	approximate value of h	[L]
$\underline{k}$	absolute permeability or specific permeability tensor	$[L^2]$
$\underline{K}$	hydraulic conductivity or permeability	[L/T]
k_f	hydraulic conductivity of fracture	[L/T]
k_s	hydraulic conductivity of skin	[L/T]
L_f	fracture length	[L]
m_c	specific fluid mass capacity	$[M/LL^3]$
M_c	fluid mass capacity of an element with volume V	[M/L]
M_{nm}	magnitude of mass transfer into subdomain n from subdomain m	[M]
M_w	mass of water contained in a volume element of bulk volume V	[M]
n	porosity	[1]
$\vec{n}$	a unit outer normal of the surface segment dΓ	[1]
$\vec{n}_z$	unit vector parallel to z axis	[1]
p	pore fluid pressure	$[M/LT^2]$
$\vec{q}$	specific flux fector of Darcy velocity	$[L^3/T]$
$\vec{q}_r$	vector flux density of water relative to the solid grains of the porous medium	$[L^3/T]$
{Q}	vector of source terms	
r_s	radius of skin	[L]
r_w	radius of well	[L]
S	saturation	[1]
s_s	specific storage	[1/L]
s_y	specific yield or effective porosity	[1]
t	time	[T]
v	prescribed specific flux	[L/T]
V	bulk volume of a volume element	$[L^3]$
V_s	volume of solids	$[L^3]$
V_v	volume of voids	$[L^3]$
w_f	fracture width	[L]
z	elevation	[L]
α	volumetric compressibility of soil skeleton (synonymous with m_v of soil mechanics literature)	$[LT^3/M]$
β	volumetric compressibility of water	$[LT^2/M]$
γ_w	specific weight of water	$[M/L^4T^2]$
Γ	boundary surface of a volume element v	$[L^2]$
θ	volumetric moisture content	[1]
λ	weighting factor for backward differencing	[1]
ξ	elevation of the freesurface above the base	[L]
ρ_w	mass density of water	$[M/L^3]$
σ	total stress on soil skeleton	$[M/LT^2]$
σ'	effective stress on soil skeleton	$[M/LT^2]$
χ,χ'	parameter relating pore fluid pressure and effective stress	[1]
ψ	pressure head	[L]
ψ_A	air entry value	[L]
ψ_w	wilting coefficient of root system	[L]